ACS APPLIED BIO MATERIALS

www.acsabm.org
Article

Assessment of Cellulose Nanofiber-Based Elastase Biosensors to Inflammatory Disease as a Function of Spacer Length and Fluorescence Response

Michael W. Easson,*,§ Jacobs H. Jordan,§ J. Vincent Edwards,* Nicolette T. Prevost, Rebecca A. Dupre, Matthew B. Hillyer, Isabel M. Lima, and Sunghyun Nam

Cite This: ACS Appl. Bio Mater. 2024, 7, 1490−1500

Read Online

ACCESS | Metrics & More | Article Recommendations | Supporting Information

ABSTRACT: Inflammatory disease biomarker detection has become a high priority in point-of-care diagnostic research in relation to chronic wounds, with a variety of sensor-based designs becoming available. Herein, two primary aspects of biosensor design are examined: (1) assessment of a cellulose nanofiber (CNF) matrix derived from cotton ginning byproducts as a sensor transducer surface; and (2) assessment of the relation of spacer length and morphology between the CNF cellulose backbone and peptide fluorophore as a function of sensor activity for porcine pancreatic and human neutrophil elastases. X-ray crystallography, specific surface area, and pore size analyses confirmed the suitability of CNF as a matrix for wound care diagnostics. Based upon the normalized degree of substitution, a pegylated-linker connecting CNF transducer substrate to peptide fluorophore showed the greatest fluorescence response, compared to short- and long-chain alkylated linkers.

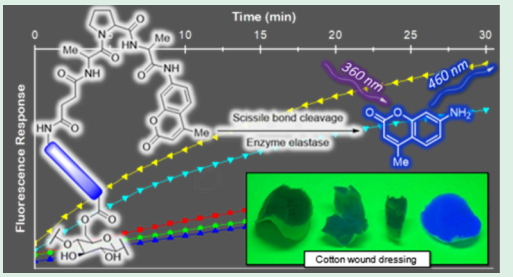

KEYWORDS: *elastase, biosensor, cellulose, nanofiber, proteases, inflammation, fluorescence*

INTRODUCTION

Cellulose is a biocompatible biopolymer made up of repeating 1−4 glycosidic linkages between glucose residues that possess reactive hydroxyls that can be derivatized to covalently append biologically active molecules. Cellulose, in nanoscopic forms as cellulose nanocrystals (CNCs) and cellulose nanofibers (CNFs) collectively referred to as nanocellulose, are effective as a transducer surface for detection of clinically relevant levels of protease.[1] These nanocellulose materials are low-cost and have high surface areas, which allow for a greater number of binding sites for biological molecules with higher specificity and sensitivity. The number of functional properties uncovered for nanocellulose's use as a sensor transducer surface has grown in recent years to include a range of mechanical and molecular design motifs and sensitivities.[2,3] Nanocellulose has been a platform for biosensing, drug delivery, and tissue engineering singularly or in combination with other molecules and polymers.[4−9] Recent improvements on the biocompatible properties of nanocellulose for use in biological systems have been reported, and numerous efforts continue to elucidate its potential as a wearable sensor for use in diagnostic, drug delivery and medical applications as "intelligent dressings".[3,10]

The first reported "intelligent dressing" was based on the ability to sense and modulate the release of moisture from a wound bed.[11] Since then, advances in material properties and most recently in point-of-care diagnostics holds promise to revolutionize healthcare by assessment of health status and disease onset using noninvasive methods.[12,13] This is especially the case with sensors and imaging to promote wound healing using biochemical and cellular markers.[14] One approach involves developing sensors that can be combined with protease-modulating dressings to help guide treatment and dressing changes.[15,16] Protease biosensors incorporate two critical components: (i) a biomolecule, or binding substrate, and (ii) a transducer surface (e.g., nanocellulose).[6] Conjugation of the substrate molecules with the transducer surface forms the apex of activation—sensor activity triggered by a biochemical event that gives rise to a detection signal. The interface of a biosensor with the protease-modulating dressing is effective and sensitive in the detection of chronic wound proteases with both colorimetric and fluorescent approaches.[1,17,18]

Biosensor mechanism design may be defined as the interface of a molecular or receptor-recognition property with cellular or biochemical activity, triggering a "biomolecular switch" that in turn is connected with a detector signal. Biosensors can generally be divided into electrical, optical, and mechanical,

Received: September 29, 2023
Revised: December 11, 2023
Accepted: January 23, 2024
Published: February 20, 2024

https://doi.org/10.1021/acsabm.3c00885
ACS Appl. Bio Mater. 2024, 7, 1490−1500

Scheme 1. General Scheme for Cleavage of Scissile Bond and Detection of 7-Amino-4-Methyl Coumarin[a]

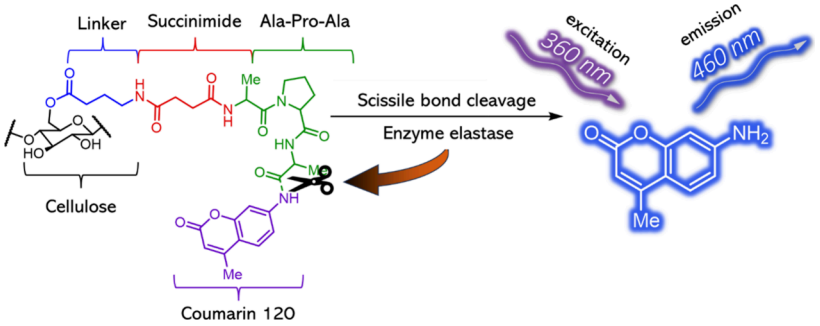

[a]General scheme for cleavage of scissile bond of CNF-Linker-Suc-APA-AMC substrate is shown with linker ii (biosensor 2).

Scheme 2. General Synthesis of CNF-PEP Transducers

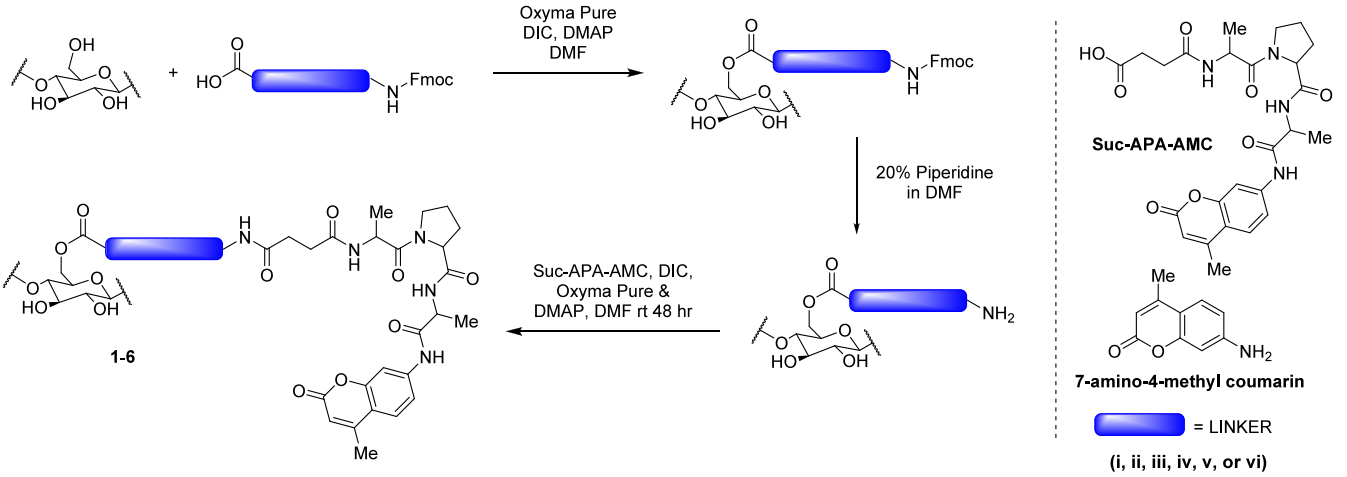

which include a wide range of detector technologies: colorimetric, fluorescent, bioluminescent, electrochemical, piezoelectric, quartz microbalance, acoustic, and conductometric signals.

The "biomolecular switch" may be defined by a range of bioactive molecules or biological responses ranging from pH changes to enzymatic or cellular sources. Detectors have been adapted to matrices that function at varying levels of sensitivity based on wavelength selectivity and sensitivity of resolution within the electromagnetic spectrum. The present research involves this biomolecular approach utilizing fluorescent detection technology in response to an elastase cleaving the scissile bond of a coumarin-based substrate (Scheme 1).

Human Neutrophil Elastase (HNE) is a 218 amino acid residue serine protease and a destructive enzyme involved in phagocytosis.[19] Elastases like HNE have been implicated in the destructive degradation of elastin, collagen, proteoglycan and other connective tissue proteins[19−21] and are typically found at elevated levels in chronic wounds, which contributes to a myriad of chronic illnesses.[17,22] Porcine Pancreatic Elastase (PPE) is often used to study elastase activity for human elastases, including human leukocyte elastase. Both HNE and PPE share 43% sequence homology[23] and have a proline-binding domain with a common recognition motif that is sensitive to electrophilic ketones.[20,24] This is regularly accomplished through the aid of fluorescent probes, wherein a fluorophore such as 7-amino-4-methylcoumarin (AMC) is attached to the tripeptide binding domain through a scissile bond and conjugation of AMC via the amino group to the tripeptide results in fluorescent quenching.[25] The enzymatic cleavage of the scissile bond by the elastase gives rise to an increase in the fluorescence signal due to free AMC in solution, which can be used to quantify the enzymatic activity of the elastase.

Serine proteases such as those described above have a central role in a wide array of inflammatory diseases that overlap in their pathology with chronic wounds.[26] Whereas previous studies for protease detection have shown varying degrees of affinity with dependence on linker length,[27−29] to date, no studies have addressed the role of spacer length and design in the context of biosensor to nanocellulose surface relationship. Prior studies utilized long-chain (up to 10 000 MW) polyethylene glycol (PEG) repeat units or short peptide units to prepare self-assembled monolayers for analyte detection on gold surfaces, typically by surface plasmon resonance or quartz crystal microbalance for piezoelectric response.[27,28] In a separate example, an electrochemical assay used a gold substrate and an eight-carbon aliphatic linker, or a PEG moiety containing 2−12 repeat units, to detect bovine serum albumin (BSA) and trypsin. In that context, this study employs cotton cellulose as a nanocellulose-based substrate for both neutrophil and pancreatic elastases. The relationship between the substrate peptide defining the sensor and the conjugated transducer surface defined by the nanocellulose composition was examined as a function of the hydrophobic/hydrophilic spacer length.

https://doi.org/10.1021/acsabm.3c00885
ACS Appl. Bio Mater. 2024, 7, 1490−1500

Chart 1. Linkers Used in the Synthesis of Biosensors/Transducers to Investigate Structure−Function Relationship

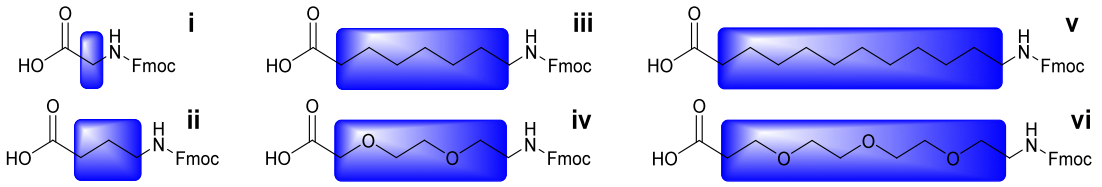

Table 1. Elemental Analysis Results and Peptide Composition of Transducers

Sensor	Linker	$N_{\%}$[a]	Calcd. [M][b] (m/z)	Q-TOF-MS[c] [M + H]$^+$ (m/z)	$N_{\%}^{Pep}$[d]	N_{factor}[e]	[Peptide] (μg/mg)[f]	DS[g] (%)
1	(**i**) Gly	0.38	571.23	572.23	12.25%	8.16	30.6	0.89
2	(**ii**) Gaba	0.16	599.26	600.26	11.68%	8.56	13.7	0.38
3	(**iii**) 8-Aoc	0.34	655.32	656.32	10.68%	9.36	35.6	0.81
4	(**iv**) (PEG)	0.39	659.28	660.29	10.62%	9.42	36.3	0.92
5	(**v**) 12-Ado	—[h]	711.38	712.39	9.84%	10.16	—[h]	—[h]
6	(**vi**) $(PEG)_2$	0.11	717.32	718.33	9.76%	10.25	10.8	0.25

[a]$N_{\%}$ is the nitrogen content determined from elemental analysis. [b][M] is calculated exact mass for the full biosensor Suc-APA-AMC plus the linker and used to determine $N_{\%}^{Pep}$. [c]The values reported were detected by liquid chromatograph-quadrupole time-of-flight mass spectrometry (Q-TOF LC/MS) as the singly charge protonated species $[M+H]^+$. [d]$N_{\%}^{Pep}$ is the calculated elemental composition of the peptide fragment including linker. [e]The N_{factor} is the reciprocal of the $N_{\%}^{Pep}$. [f]The peptide concentration (μg/mg) is determined from the total concentration of nitrogen and includes the linker. [g]D.S. is the degree of substitution calculated by the Touzinsky and Gordon method. [h]The elemental results were below the limit of detection.

RESULTS AND DISCUSSION

Biosensor Synthesis. Biosensors were prepared by solid-phase peptide synthesis, whereby the CNFs acted as the solid phase support and transducer surface using modifications to methods employed previously (Scheme 2).[30] Ester formation via coupling of the Fmoc-protected linker with *N,N′*-diisopropylcarbodiimide (DIC) was aided by ethylcyanoglyoxylate-2-oxime (Oxyma Pure) in dimethylaminopyridine (DMAP) and *N,N*-dimethylformamide (DMF). Subsequent deprotection of the Fmoc group with 20% piperidine in DMF proceeded cleanly to afford the free amine, to which the N-succinyl-Ala-Pro-Ala-7-amino-4-methylcoumarin (Suc-APA-AMC) peptide fragment was coupled through amide bond formation to give transducers **1**−**6** (Supporting Information: Scheme S1−S6 and Figures S2−S13).

The specific linkers chosen for this work (Chart 1) were selected to test the structure−activity relationship. Specifically, transducer **1** with a glycine linker (**i**) was selected based on its known activity for human neutrophil elastase (HNE),[30] while linkers **ii**, **iii**, and **v** represent linkers with an additional two, four, or ten methylene groups as spacers between the CNF surface and the peptide fragment to give transducers **2**, **3**, and **5**, respectively. Linkers **iv** and **vi** were selected for transducers **4** and **6** as structural analogues to linkers **iii** and **v** but containing poly(ethylene glycol) (PEG) moieties whereby oxygen replaces either two or three of the methylene groups present in the linker to explore hydrophobicity and solvency effects.

Nitrogen Analysis and Degree of Substitution (DS). A corrected nitrogen conversion factor[31] was used to calculate the percent of peptide present in each biosensor based on the elemental composition of the cleaved linker unit detected by Q-TOF-LC/MS. The results from elemental analysis, detected mass to charge (m/z) and $Peptide_{\%}$ are shown in Table 1. The results from elemental analysis and peptide composition were used to determine the degree of substitution (DS) of the CNFs with the peptide fragments using eq 2. Importantly, since the attached linker only contains a single nitrogen atom, in all cases the elemental results for the intermediate products were below the instrument's limit of detection (LOD ≥ 0.10%); thus, the results reported in Table 1 were determined using the total nitrogen content of final products **1**−**6** (CNF-Linker-Suc-APA-AMC) and the calculation of the degree of substitution includes the nitrogen contribution from the attached linker (**i**−**vi**) group. Importantly, both the final product and intermediate in the case of **5** gave $N_{\%}$ values ≤0.10%; therefore, the data are not reported. This is likely caused by the poor reactivity of the longer chain aliphatic substrate due to steric constraints from agglomeration of the CNFs and/or aggregation of the reagents in the polar solvent, which may limit access of the hydroxyl nucleophile of the CNFs during the peptide synthesis. The steric hindrance is supported by the low reactivity and substitution of **6**, which also bears a longer chain; however, since the ethylene glycol groups are inductively withdrawing and promote solubility and dispersion of the linker in solution, the carboxylate is more reactive and greater substitution was observed.

Interestingly, when the aliphatic group was somewhat smaller as is the case with linkers **3** and **4**, this was not observed, and similar reactivity was observed between linkers **3** and **4**, which led to a comparable degree of substitution. Further exploration of reaction conditions, particularly with regards to reaction temperature, peptide coupling reagent selection, and stoichiometry, could lead to an increase in the DS for specific linkers, resulting in an increase in $N_{\%}$ in products that are below the LOD.

For further characterization of the physical properties of the cotton gin mote (CGM) cellulose nanofibers (CNFs), samples were analyzed by powder X-ray diffraction (XRD) (Figure 1a). The samples exhibited a diffraction pattern corresponding to the cellulose Iβ allomorph with predominant reflections observed at 14.7°, 16.4°, 22.7°, and 34.4° 2θ, which correspond to the (1−10), (110), (200), and (004) lattice planes. The percentage of crystalline cellulose Iβ was calculated at 71% and the average crystallite size was 74.7 Å. The refined unit cell dimensions gave a unit cell volume of 674 Å^3 (a =

https://doi.org/10.1021/acsabm.3c00885
ACS Appl. Bio Mater. 2024, 7, 1490−1500

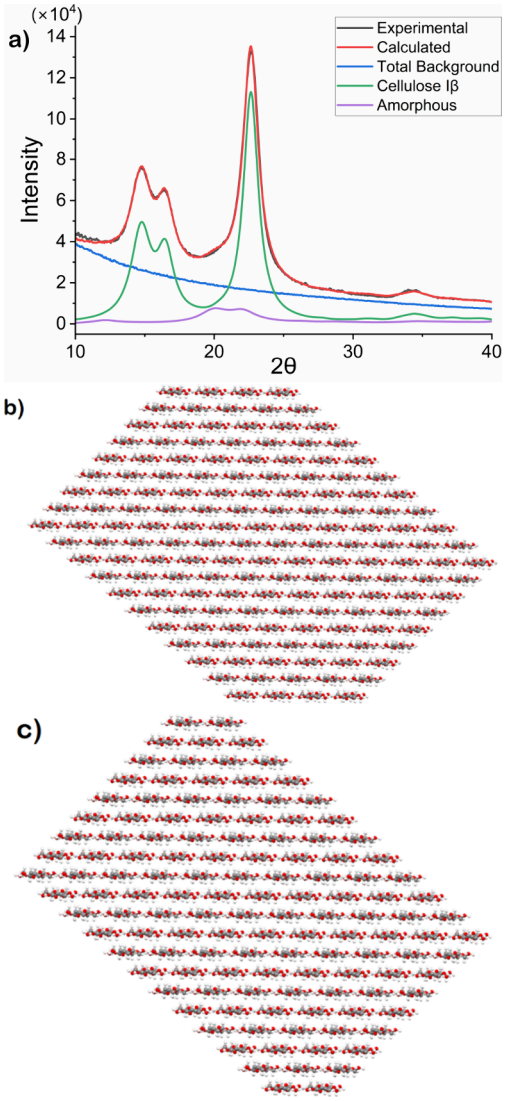

Figure 1. (a) Powder X-ray diffraction pattern of cellulose nanofibers and Rietveld refinement showing cellulose Iβ and amorphous components; (b) general model for cellulose Iβ crystallite from average crystallite size; and (c) model based on the (200), (1−10), and (110) lattice plane dimensions.

7.89, b = 8.20, c = 10.42 Å), which is slightly larger than the refined unit cell dimensions reported by Nishiyama et. al and those used previously.[22,32] The corresponding d-spacings and dimensions of the cellulose Iβ crystallite along each lattice plane and number of cellulose layers per crystallite (Supporting Information, Table S1) were used to construct models of the cellulose crystallites from a single chain layer of glucose residues.

The general model for a cellulose crystallite with an average crystallite size of 74.7 Å gives a crystallite with 19 layers with respect to the (200) lattice plane and 156 glucose chains (Figure 1b), whereas the specific model based on the crystallite sizes determined through Rietveld refinement gives a model with 21 layers and 128 chains (Figure 1c). While this model has fewer overall chains, there are more exposed chains to the hydrophilic surface of the (1−10) and (110) lattice planes. The crystallite size and unit cell dimensions remain constant during the relatively mild conditions employed for the peptide coupling reactions.[1,22]

Thus, the same model for CNFs can be applied to each peptide analogue (**1**−**6**) and the degree of substitution (DS) per crystallite layer can be readily determined from the degree of substitution calculated using eq 2, and the crystallite volume (21.6 nm^3), which was determined from the number of chains in the crystallite model divided by two and multiplied by the half unit cell volume from the refined unit cell dimensions (Table 2).

Table 2. Degree of Substitution Per Crystallite and Corresponding Number of Sensors Per Unit Volume

Sensor	DS (%)[a]	DS per crystallite[b]	Sensors per volume[c]	Sensors per μm^3 (×10^6)
1	0.89	1.14	1.26	53
2	0.38	0.48	0.53	22
3	0.81	1.04	1.14	48
4	0.92	1.18	1.30	55
5	—[d]	—[d]	—[d]	—[d]
6	0.25	0.31	0.35	15

[a]D.S. is the degree of substitution calculated by the Touzinsky and Gordon method. [b]The DS per crystallite is determined from the number of cellulose chains per crystallite × the DS. [c]The sensors per volume is related to the volume of sensors that can share the same space as a reference crystallite from cellulose filter paper.[22] [d]The elemental results were below the limit of detection.

Raman Spectroscopy. The Raman spectrum for cellulose nanofibers (Figure 2) exhibit distinctive Raman active vibrational modes.[33,34] Notably, the signals at 1116 and 1331 cm^{-1} correspond to the ν(C−O−C) bending of the glycosidic linkage vibrational mode, and the peak at 1088 cm^{-1} is characteristic of the ν(C−O−C) stretching vibrational mode. Synthesis of Fmoc-terminated linker to CNFs was confirmed by the appearance of two peaks, one at 1580 cm^{-1} and the other at 1610 cm^{-1},[35] where the peak at 1610 cm^{-1} is sharper and gives about twice the intensity as the broad peak observed at 1580 cm^{-1}. These spectroscopic features are lost upon deprotection of the linker, and finally, new signals are observed upon derivatization of the amine terminus with a coumarin moiety. These two broad peaks with similar intensity arise at 1580 and 1615 cm^{-1} corresponding to ν(C═C) stretching and conjugated ν(C═O)/ν(C═C) stretching, respectively.[36] These peaks are most pronounced in sensors **1**, **3**, and **4**, which have the greatest degree of substitution among all derivatives.

Specific Surface Area and Pore Size Analyses. Specific surface area (SSA) and pore size analyses are important for material surface characterization. Porous materials are characterized by their pore volume and may fall into different regimes depending on the diameter of the pores, either macroporous (>50 nm), mesoporous (2−50 nm), or microporous (<2 nm). For CNFs, the specific surface area ($m^2 \cdot g^{-1}$) was determined using multipoint BET (Brunauer−Emmett−Teller) measurements, and pore size distribution was estimated using a solid density functional theory model applied to physical adsorption of nitrogen. The model has been used for predicting adsorption/desorption isotherms in nanopores of different geometries over a wide range of pore sizes (0.5−100 nm) and for calculating pore size distributions from adsorption isotherms.[37] The method can be ideal for describing the actual pore size distribution in porous sorbents, particularly in the micropore and narrow mesopore regions,[38,39] and has been

https://doi.org/10.1021/acsabm.3c00885
ACS Appl. Bio Mater. 2024, 7, 1490−1500

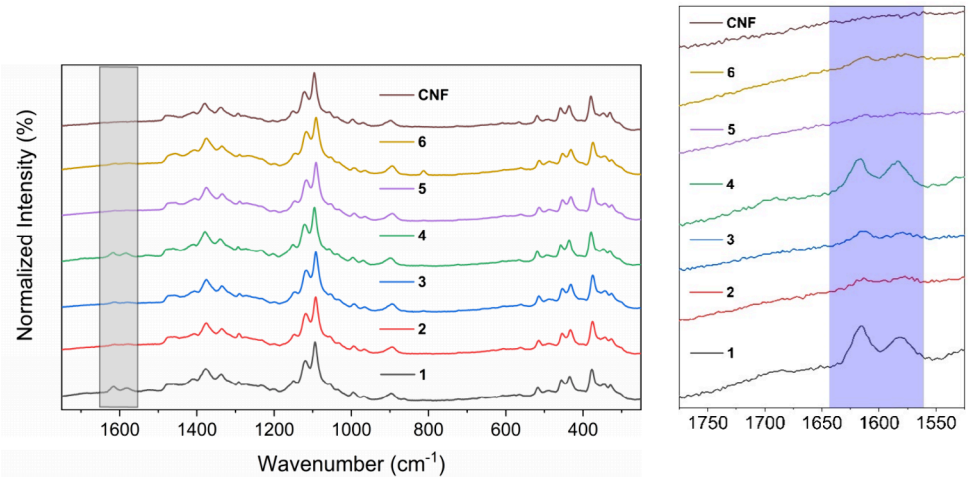

Figure 2. Raman spectra for CNFs and conjugated biosensor/transducers. The area shown in gray is expanded at right. The highlighted region shows Raman peaks associated with 4-amido-7-coumarin in the biosensor unit.

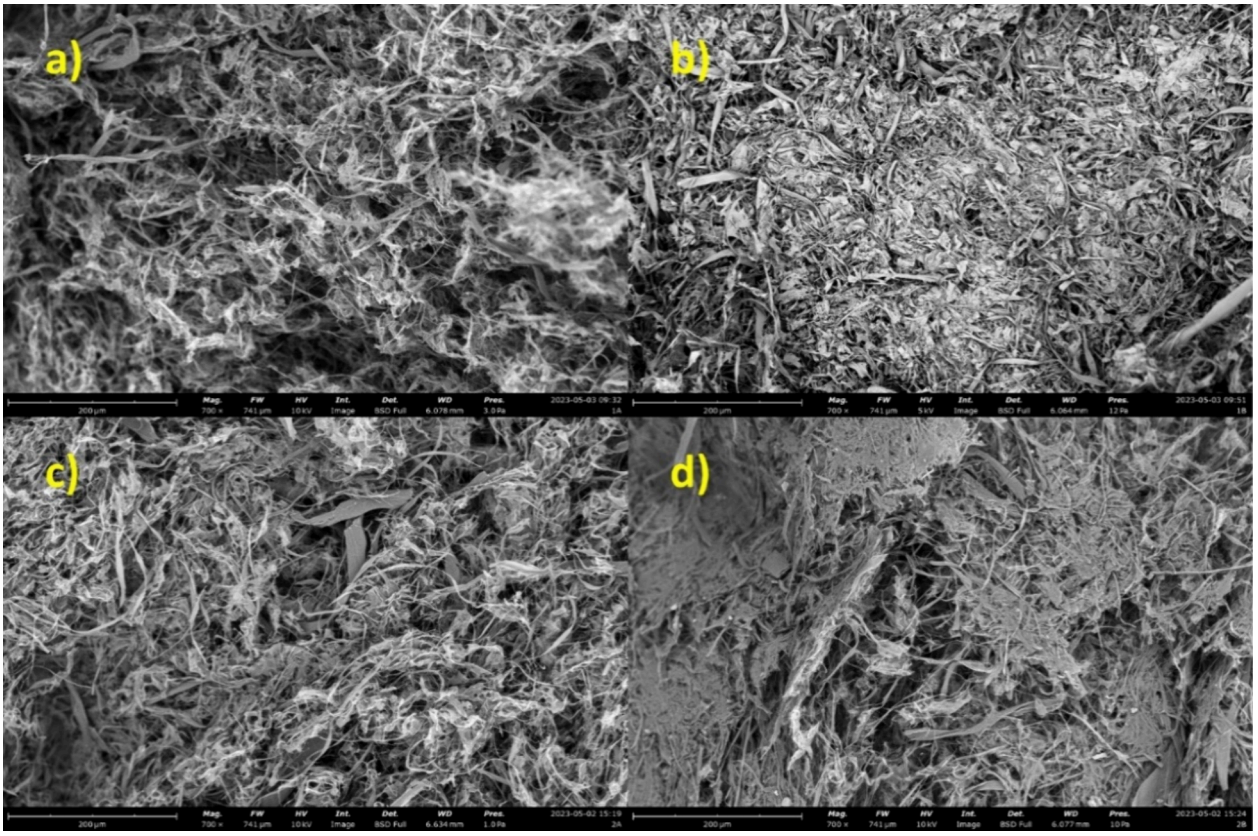

Figure 3. SEM images (700× magnification) of CNF aerogels (a, c) before and (b, d) after BET analysis: (a) CNF aerogel prepared from 0.36 wt % suspension, (b) CNF aerogel from 0.36 wt % suspension after drying at 150 °C and BET analysis, (c) CNF aerogel prepared from 0.70 wt % suspension, and (d) CNF aerogel from 0.70 wt % suspension after drying at 150 °C and BET analysis.

widely applied to study cellulosic materials and composites.[40−42]

For BET analysis two different concentrations of CNFs from cotton gin motes were first lyophilized and then the obtained aerogels were analyzed for specific surface area[43] and total pore volume (Figures S16 and S17); thermogravimetric analysis (TGA) was used to analyze CNFs (Figure S15) to determine their thermal stability prior to BET analysis. The total pore volume and specific surface area were found to be concentration dependent. When the CNF concentration was 0.36% (w/w), the pore volume was 54.3 $mm^3\ g^{-1}$ and the specific surface area was 15.54 $m^2\ g^{-1}$. Increasing the concentration to 0.70% (w/w) gave a pore volume of 49.8 $mm^3{\cdot}g^{-1}$ and a surface area of 12.44 $m^2\ g^{-1}$. These results for CNFs are significantly improved compared to cellulosic fibers[40] and comparable to other nanocellulose aerogels.[42] Further, these results indicate that the pore volume and surface area may be attenuated by increasing the concentration of CNFs leading to a decrease in specific surface area and total pore volume. This suggests that the concentration of CNFs is

https://doi.org/10.1021/acsabm.3c00885
ACS Appl. Bio Mater. 2024, 7, 1490−1500

critically important for reaction optimization,[44] maximum derivatization of the surface area, and affects assembly and redispersibility.[45,46] Moreover, CNF concentration and accessible surface area affects the enzyme accessibility for the substrate.[1,17,47]

Figure 3 shows the SEM images of the CNF samples taken at low (700×) magnification. The low magnification images show the overall morphology and highly porous network of the lyophilized samples.

Specifically, Figure 3a and Figure 3c show a highly porous structure of the CNFs prepared prior to BET analysis at suspension concentrations of 0.36% and 0.70% (w/w), respectively. In contrast, the structures presented in Figure 3b and Figure 3d after BET analysis appear denser than those presented prior to analysis, albeit the same porous structure is visible. Images taken at greater magnification (Supporting Information Figure S18) reveal the presence of a mesoporous structure within the CNF aerogel.

Progress Curves. To further analyze the synthesized products, progress curves for the enzymatic cleavage of the scissile bond were collected for the free sensor unit (Suc-APA-AMC) and the biosensors upon the addition of Porcine Pancreatic Elastase (PPE) or Human Neutrophil Elastase (HNE) (see Supporting Information Figures S20–S33 for details). For comparison, it should be noted that **1**, **3**, and **4** had comparable degrees of substitution and the overall order for the degree of substitution of the biosensor onto the substrate was **4** ≈ **1** > **3** > **2** > **6** > **5**; thus, if the kinetic response of the enzyme is identical for each linker, the order of activity would follow the same trend as observed for the degree of substitution. This was not the case (Figure 4; see Supporting Information Figure S34 for more details).

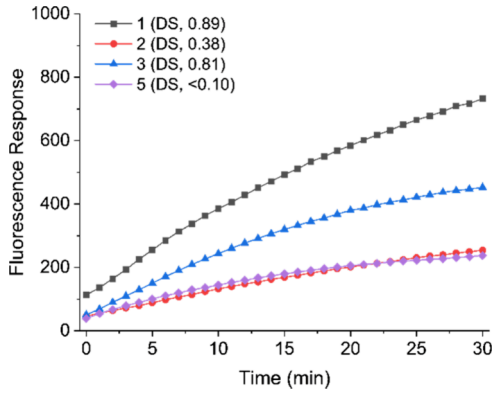

Figure 4. Progress curves for aliphatic linkers (**1**, **2**, **3**, and **5**) in the presence of 1.5 U/mL of PPE (50 μL) as a function of time. The DS for each linker is included in the legend for context.

For PPE (Figure S34a), with increasing aliphatic chain length (Figure 4), a decrease in PPE activity for the substrate was observed and the order of activity of PPE toward the substrate was **1** > **3** > **2** ≈ **5**.

This was most evident for **2**, which, while significantly more substituted (DS = 0.38), showed a similar response toward PPE as did **5**, where the DS was undetectable based on nitrogen analysis. The fact that **3** with the intermediate linker length (C_8) displayed an increased fluorescence response is not surprising considering its greater DS value compared to those of **2** and **5**.

Yet with a comparable DS value to **1**, the activity was significantly lower, suggesting the longer aliphatic chain actually serves to decrease affinity of the enzyme for the substrate despite the greater steric accessibility. A similar trend was observed for HNE (Figure S34b) where **1** > **3** > **2** > **5**.

In contrast, both of the biosensors containing the poly-(ethylene glycol) (PEG) linkers (**4** and **6**) displayed improved activity compared to the aliphatic chain linkers, likely due to enhanced accessibility of the PEG linker, as it can be readily solvated in the aqueous solution. It is interesting to note, however, that while the apparent activity of **4** toward both PPE and HNE exceeds all other synthesized substrates, the activity of **6**, based solely on the reaction progress curves is lower than anticipated. This lower activity can be largely ascribed to the lower degree of substitution for **6** compared to **4**. However, once the reaction progress curves are normalized relative to the degree of substitution of each substrate (Figure 5), the relative

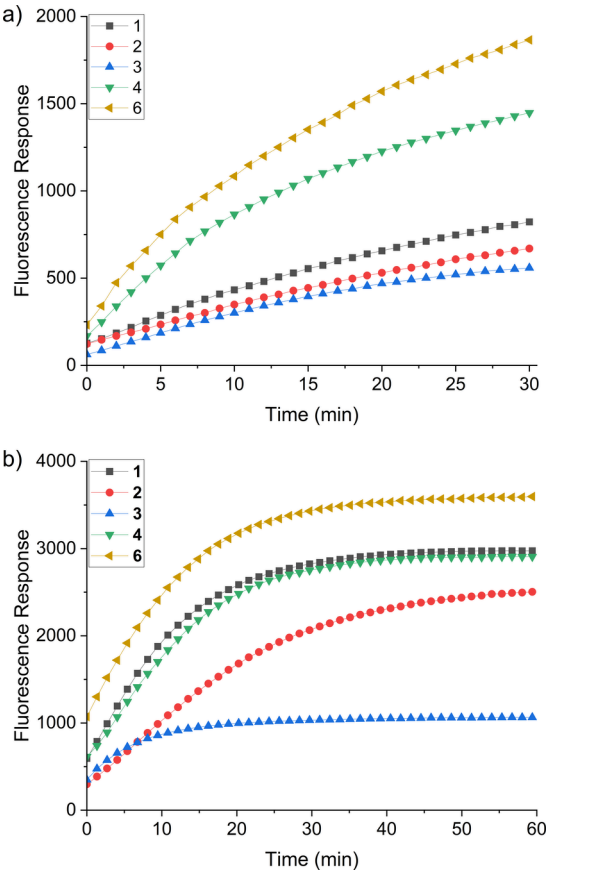

Figure 5. Normalized curves obtained by dividing the fluorescence response by the degree of substitution per 100 residues for (a) biosensor substrates in the presence of 1.5 U/mL PPE as a function of time, and (b) biosensor substrates in the presence of 1.2 U/mL HNE as a function of time. Progress curves for **5** are not shown since the degree of substitution of the substrate could not be accurately determined.

activity of each substrate becomes clearer. Hence, the activity of HNE and PPE toward biosensor **6** was the greatest among the linkers examined while **3** was the least active transducer. As can be seen from the normalized reaction progress curves (Figure 5), the most active substrates contained the poly-ethylene glycol repeat unit, where for linker **6** the fluorescence response was nearly three times that for the Gly-substituted **1**

https://doi.org/10.1021/acsabm.3c00885
ACS Appl. Bio Mater. 2024, 7, 1490−1500

Table 3. Concentration of Available Peptide, Extent of Reaction, and Activity of Elastase for Each Biosensor Transducer

		PPE			HNE		
Sensor	[Pep] (μM)[a]	ξ (%)	FR(d/dt) (s^{-1})	k_{app} (s^{-1})	ξ (%)	FR(d/dt) (s^{-})	k_{app} (s^{-1})
Suc-APA-AMC	165	98	1.5×10^{-3}	1.2×10^{-3}	99	1.0×10^{-3}	6.8×10^{-4}
1	357	17	5.3×10^{-4}	4.4×10^{-4}	69	1.3×10^{-3}	1.0×10^{-3}
2	153	14	3.9×10^{-4}	3.4×10^{-4}	39	7.2×10^{-4}	6.4×10^{-4}
3	324	10	7.5×10^{-4}	5.5×10^{-4}	15	1.7×10^{-3}	1.5×10^{-3}
4	367	40	1.0×10^{-3}	4.6×10^{-4}	67	1.4×10^{-3}	1.0×10^{-3}
5	95[b]	16	9.9×10^{-4}	6.2×10^{-4}	17	2.3×10^{-3}	2.3×10^{-3}
6	100	23	9.1×10^{-4}	8.3×10^{-4}	53	9.1×10^{-4}	8.3×10^{-4}

[a][Pep] is the calculated maximum concentration of peptide (Suc-AMA-AMC) bound to CNFs per reaction well based on the degree of substitution of each CNF biosensor. [b]Based on an assumed degree of substitution of 0.10, which is the limit of detection for the analysis.

for PPE. Similarly, **4** displayed nearly twice the normalized fluorescence response compared to the Gly unit of **1** for PPE and was significantly more active than the comparable linker with the aliphatic chain (**3**). The order of activity for PPE was then **6** > **4** > **1** > **2** > **3**, for which a similar trend was observed for HNE: **6** > **4** ≈ **1** > **2** > **3.**

To further understand the relative activity of the enzyme for the different biosensor substrates, the non-normalized reaction progress curves were fit to the Michaelis−Menten equation, monitoring both the increase in fluorescence intensity and the appearance of product concentration over time by numerical modeling the whole course of the enzymatic reaction rather than using only initial rates (see the Supporting Information for details).[48−50] This was due to the relatively low substitution of peptide on the substrates and the working concentration of the enzyme necessary to achieve reliable spectroscopic data, making the usual modeling with initial rates to determine V_{max} and K_m untenable. This modeling over the entire progress curve gave the observed rate constants reported in Table 3.

Generally, the apparent rate constants monitoring the accumulation of AMC were somewhat lower than the rate of change in the fluorescence response. The maximum concentration of peptide in the reaction well bound to each CNF substrate ([Pep]), based on DS calculations (Table 1) is presented in Table 3 with the extent of reaction (ξ) obtained from monitoring the progress curves for the appearance of product. Generally, PPE was less effective than HNE at consuming the available substrate and liberating free AMC only cleaving 10−40% of the available scissile bonds, while HNE was more effective, liberating 15−69% of bound AMC. The somewhat greater availability of peptide substrate on **1**, **3**, and **4**, contributed to the larger observed rate, which was substrate-concentration dependent. Both biosensor **3** with a high degree of substitution and **5** with a lower degree of substitution reached a plateau in the fluorescence response—and liberated AMC—very early in the reaction progress curve. This can likely be explained by the poorly solvated hydrophobic aliphatic chains of the linkers, making the substrate less accessible. In contrast, the well-solvated linkers of substrates **4** and **6** proceeded to a greater extent and gave large rate constants.

CONCLUSIONS

Six fluorophore biosensors were each synthesized in three steps by combining a cellulose nanofiber substrate, a hydrophobic or hydrophilic linker, and a tripeptide-coumarin synthetic motif. Intermediates and final products were confirmed by Raman and LC/MS spectroscopy. Results showed that well-solvated, hydrophilic biosensors containing pegylated units in their respective linkers interacted better with PPE and HNE elastases and released higher concentrations of AMC fluorophore than poorly solvated aliphatic biosensors when the fluorescence response was normalized for the degree of substitution.

Increasing aliphatic linker length contributed to a poorer fluorescence response in both elastase assays. Fits of the fluorescence response and the calculated concentration of the liberated AMC fluorophore analyte gave approximately equal values for the first-order rate expression. Cellulose nanofibers offer a promising transducer substrate for appending point-of-care diagnostic biosensor molecules. X-ray crystallography, specific surface area, and pore size analyses confirm that CNFs are a highly crystalline medium with considerable surface area and pore size volume that enable opportunities for biosensor application. Future investigations should be performed to model enzyme/biosensor molecular interactions and further elucidate their kinetic profiles.

EXPERIMENTAL SECTION

General. Acetonitrile and trifluoroacetic acid (TFA) were purchased from Fisher Scientific (Pittsburgh, PA) as LC/MS grade. Sodium hydroxide, sodium chlorite, acetic acid, anhydrous *N,N*-dimethylformamide (DMF), isopropanol, ethylcyanoglyoxylate-2-oxime (Oxyma Pure), *N,N′*-diisopropylcarbodiimide (DIC), triisopropylsilane (TIPS), dimethylaminopyridine (DMAP), Fmoc-Gly-OH, Fmoc-GABA−OH, Fmoc-8-Aoc−OH, Fmoc-12-Ado−OH, Fmoc-NH-(PEG)-COOH, and Fmoc-NH-$(PEG)_2$-COOH were purchased from Millipore-Sigma (Burlington, MA). N-Succinyl-Ala-Pro-Ala-7-amino-4-methylcoumarin (Suc-APA-AMC) was purchased from Bachem (Torrence, CA). Human neutrophil elastase (HNE) and porcine pancreatic elastase (PPE), purified and lyophilized, were purchased from Innovative Research (Novi, MI). All chemicals and reagents were used as received without further purification. Nitrogen elemental analysis was performed by the Midwest Microlab (Indianapolis, IN).

Preparation of Nanocellulose Fibers. Cellulose nanofibers were isolated from cotton gin motes (CGM) using a procedure previously reported.[51] CGM were mechanically ground to <20 mesh with a Wiley mill (E3300, Eberbach Corp., Belleville, MI). The obtained dry powder was treated for 2 h at 70 °C with a 4% (w/w) sodium hydroxide (NaOH) solution at a fiber-to-liquor ratio of 1:20 (w/v). Afterward, the fibers were washed with deionized water until a pH of 6−7 eluant was achieved. The fibers were then exhaustively bleached (fiber to liquor ratio of 1:20 (w/v)) three times at 75 °C for 2 h with an acidified sodium chlorite ($NaClO_2$, 0.50%, w/v) solution containing 1.0% acetic acid (v/v). The cellulose was recovered after thoroughly washing with deionized water and then dried to a constant mass at 70 °C. Then, bleached cellulose fibers were suspended in deionized water using an Ultra-Turrax (T25, IKA Works, Inc., Wilmington, NC) mechanical homogenizer to obtain a 1% (w/w) cellulose slurry. The slurry was processed with a rotor-stator mixer

https://doi.org/10.1021/acsabm.3c00885
ACS Appl. Bio Mater. 2024, 7, 1490−1500

(Silverson L5M-A, East Longmeadow, MA) fitted with a square hole high shear screen and a set rotational speed of 8,800 rpm for 15 min to reduce particle size and prepare a homogeneous suspension. The cellulose suspension was then subjected to high-shearing forces using a high-pressure homogenizer (Microfluidizer M-110P, Microfluidics Corp., Newton, MA). The slurry was injected, and the suspension was pumped through one 200 μm ceramic and one 87 μm diamond Z-shaped interaction chamber aligned in series for a total of five passes. After the suspension was collected, the concentration of nanocellulose fibers was adjusted as necessary, prior to analysis.

Synthesis of Biosensors (1−6). Biosensors were prepared as previously described for linker **1**,[30,47] and then by modifications to the reported procedure for linkers **2**−**6**. Briefly, for the preparation of Fmoc-linker-CNF, the CNF suspension was solvent exchanged stepwise from the aqueous suspension to isopropanol and then DMF prior to reaction. To a solution of DMAP, DIC, and Oxyma Pure in DMF was added the solvent-exchanged CNFs in DMF and the reaction stirred at rt for 48 h. The products were washed twice with isopropanol and then twice with DMF. The intermediate Fmoc-Linker-CNF compound was suspended in a mixture of DMF and Pyridine (4:1) and stirred for 15−30 min at rt under nitrogen to remove the Fmoc protective group. The NH_2-linker-CNF product was washed twice with isopropanol and then twice with DMF. Separately the Suc-APA-AMC peptide fragment, DMAP, DIC, and Oxyma Pure were suspended in DMF and the NH_2-linker-CNF in DMF (3.3 mg/mL) was added to the suspension and stirred at rt for 48 h. Upon completion, the product was washed twice with isopropanol and then dried under a vacuum to give the biosensor. Additional synthetic details can be found in the Supporting Information.

Characterization of Intermediate and Final Biosensor Products (1−6) by Raman Spectroscopy. A small sample of freeze-dried material was formed into a 7 mm flat disk using a die set (Pike Technologies, Fitchburg, WI). Each sample was placed on a glass slide and loaded into a DXR Raman spectromicroscope (Thermo Scientific, Madison, WI). The spectra were collected using an excitation wavelength of 785 nm and an output power of 20 mW. The sample was focused under a 50× confocal microscope objective and 50 μm slit width, which produces a 1.0 μm diameter collection area. Each spectrum is an average of 15 scans of 5 s acquisition time each across the spectral range of 1750 to 125 cm^{-1}.

Fluorogenic Enzymatic Activity Assay. Stock solutions of the substrates and enzyme were prepared from which subsequent working solutions were made using a phosphate-buffered saline (PBS) solution consisting of 0.1 M sodium dihydrogen phosphate (NaH_2PO_4) and 0.5 M sodium chloride (NaCl) in ultrapure water with 18.2 MΩ resistivity (Milli-Q, Millipore Sigma, MA). The pH was adjusted to 7.4 by small aliquots of either aqueous NaOH or HCl as appropriate. The fluorogenic substrate (Suc-APA-AMC) was prepared with a serial 1/2-dilution ranging from 1.00 mM to 15.6 μM as a control for the activity of the enzyme on the free substrate in solution. The biosensor stock solutions were prepared by suspending 20 mg of biosensor (**1**−**6**) in 2.00 mL of PBS, equaling a concentration of 10 mg/mL (1.00 wt % CNF biosensor). The biosensor and substrate suspensions (100 μL) were transferred to Corning black, flat bottom, polystyrene, 96-well nontreated microplates (Fisher Scientific, Pittsburgh, PA). To initiate the enzymatic reaction, 50 μL of elastase at a concentration of 1.2 or 1.5 U/mL was added to each well suspension, giving a final total well volume of 150 μL. Measurement commenced immediately at 37 °C and continued for 30 and 60 min for PPE and HNE, respectively, at 1 min intervals. The 96-well plate was shaken before each measurement for 3 s. Fluorescence measurements were recorded on a Biotek Synergy HTX multimode plate reader (Agilent Technologies, Santa Clara, CA), with an excitation wavelength of 360 nm and emission recorded at 460 nm.

Mass Spectrometry. Small portions (<8 mg) of the biosensor intermediates and products were weighed into 2 mL vials. A mixture of TFA and TIPS (100 μL, TFA/H_2O/TIPS, 95/2.5/2.5, v/v/v) was used to remove the conjugated cellulose. The mixture was vortexed for 5 s, left at room temperature for 90 min, and evaporated to dryness under a stream of N_2. Aqueous formic acid (1% formic acid, 500 μL) was added to the dried product. Filter vials (0.45 μm, PTFE) were used to remove insoluble cellulose. Aliquots of the filtered products (1.0 μL) were analyzed using an Agilent 6520 liquid chromatograph-quadrupole time-of-flight mass spectrometer (Q-TOF LC/MS, Agilent Technologies, Santa Clara, CA) equipped with a Chip Cube interface and a 1200 LC system. A water/acetonitrile gradient containing 0.1% formic acid and a Zorbax 300SB-C18 Large Capacity Chip (II) was used for chromatographic separation.

Electron Microscopy. Scanning electron microscope (SEM) images were obtained using a Phenom ProX G6 SEM (Thermo Fisher Scientific, Waltham, MA) at an accelerating voltage of 5 or 10 kV. The samples were mounted on a stub using double-sided carbon tape and coated with a 5 nm layer of gold using a LUXOR sputter coater (Aptco Technologies, Peachtree Corners, GA).

Elemental Analysis. Solid samples were submitted to Midwest Microlab (Indianapolis, IN) for nitrogen (N) analysis. Instrumental analysis for nitrogen had a limit of detection (LOD) of ≥0.10%. An adjusted nitrogen conversion factor[31] (N_{factor}) was determined based on the calculated elemental composition of the peptide fragment including linker ($N_{\%}^{pep}$), which was used to convert percent nitrogen in the biosensors to percent peptide using eq 1.

$$\text{Petide}_{\%} = N_{\%}(N_{\text{factor}}) \tag{1}$$

Where $\text{Peptide}_{\%}$ is the percentage of peptide present in the biosensor, the N_{factor} is the reciprocal of the nitrogen composition of the peptide fragment, and $N_{\%}$ is the nitrogen content from elemental analysis results. The percentage of peptide (parts per hundred) can readily be converted to the mass of the transducer on the biosensor (μg/mg) as parts per thousand.

Degree of Substitution. The degree of substitution (DS) of the biosensors was calculated based on the percent nitrogen determined with elemental analysis ($N_{\%}$) of the biosensor substrates[52] using eq 2, where $N_{\%}$ is the weight percent of nitrogen, MW_U is the molecular weight of the glucose repeat unit,[53] n is the number of nitrogen atoms in the peptide fragment and MW_a is the molecular weight added from the peptide fragment.

$$\text{DS} = \frac{N_{\%}\text{MW}_\text{U}}{14.008n - N_{\%}\text{MW}_\text{a}} \tag{2}$$

It should be noted that MW_U is the molecular weight of the repeat unit (162.14 g/mol) glucose monomer, not of glucose (180.16 g/mol), $N_{\%}$ is expressed as a percentage and MW_a is the added molecular weight of the linker, not the total molecular weight of the peptide fragment. Thus, for biosensor **1**, the molecular weight of the peptide fragment is 571.59 g/mol, the exact mass is 571.29 m/z, and the added molecular weight of the peptide fragment after the loss of water during the condensation reaction is 553.57 (g/mol). These values were used in conjunction with the number of chains in each crystallite model to calculate the degree of substitution per crystallite.

Powder X-ray Diffraction (XRD). The XRD measurements were performed by the Shared Instrumentation Facility at Louisiana State University (Baton Rouge, LA). Measurements were performed at room temperature using a spinning sample holder and Cu Kα-radiation (1.5406 Å) with a detector equipped with a 1.0 mm radial divergence slit and a 0.1 mm receiving slit. Powder diffraction patterns were acquired for lyophilized CNFs and were analyzed with the Materials Analysis Using Diffraction (MAUD) Rietveld refinement program (version 2.84) employing a pseudo-Voigt peak shape.[54] Crystallographic information files for cellulose Iβ and cellulose II were used for the crystalline and amorphous phases.[55−57] The instrumental scattering obtained from a blank sample holder was subtracted from the obtained results. Unit cell dimensions, crystallite anisotropy, preferred orientation, and background scattering using a second-order polynomial were refinable parameters. The relative percent of each phase, d-spacings, and dimensions of the crystallite size corresponding to the Miller indices for the (110), (1−10), and (200) lattice planes were extracted directly from the calculated refinement parameters.

https://doi.org/10.1021/acsabm.3c00885
ACS Appl. Bio Mater. 2024, 7, 1490−1500

Thermal Analysis. A TA Instruments Q500 thermal analyzer (New Castle, DE) was used for thermogravimetric analysis (TGA) to measure the thermograms (TG) and derivative thermograms (DTG) of the cellulose nanofibers. Samples of CNFs weighing approximately 5 mg were analyzed over the range of 30−600 °C under a nitrogen atmosphere with a gas flow rate of 10 mL min^{-1} and 10 °C min^{-1} heating ramp. Thermograms were analyzed using TA Instruments Universal Analysis 2000 software package (v. 4.5A, Waters − LLC, Newcastle, DE).

Surface Area and Pore Size Analysis. Surface area and pore structure were investigated by using a Quantachrome NOVA 2200e adsorption system (Quantachrome Instruments, Boynton Beach, FL). Lyophilized samples of CNFs were outgassed at 150 °C for 7 days under vacuum. Recommended degassing temperatures are usually 200−300 °C, however, degassing temperature of 150 °C was chosen to prevent thermally induced modification to the native material due to heat sensitivity.[58] Degassing time was significantly extended to compensate for lower degassing temperatures. Adsorption data were collected using 25 points on the nitrogen isotherm between 0.0499−0.9871 relative pressures at 77 K (−196 °C) and desorption data were collected using 12 or 25 points from 0.9871−0.04735 relative pressure at 77 K (−196 °C).

■ ASSOCIATED CONTENT

Supporting Information

The Supporting Information is available free of charge at https://pubs.acs.org/doi/10.1021/acsabm.3c00885.

Additional synthetic details, reaction schemes, Raman data, Q-TOF LC/MS data, and enzymatic progress curves are available (PDF)

■ AUTHOR INFORMATION

Corresponding Authors

Michael W. Easson − *US Department of Agriculture, Agricultural Research Service, Southern Regional Research Center, New Orleans, Louisiana 70124, United States;* orcid.org/0000-0002-2268-1922; Email: michael.easson@usda.gov

J. Vincent Edwards − *US Department of Agriculture, Agricultural Research Service, Southern Regional Research Center, New Orleans, Louisiana 70124, United States;* orcid.org/0000-0002-2620-6360; Email: vince.edwards@usda.gov

Authors

Jacobs H. Jordan − *US Department of Agriculture, Agricultural Research Service, Southern Regional Research Center, New Orleans, Louisiana 70124, United States;* orcid.org/0000-0002-0238-3864

Nicolette T. Prevost − *US Department of Agriculture, Agricultural Research Service, Southern Regional Research Center, New Orleans, Louisiana 70124, United States*

Rebecca A. Dupre − *Oak Ridge Institute for Science and Education, U.S. Department of Energy, Oak Ridge, Tennessee 37831, United States;* Present Address: U.S. Department of Agriculture, Agricultural Research Service, Southern Regional Research Center, 1100 Allen Toussaint Blvd, New Orleans, LA 70124, USA; orcid.org/0000-0002-4885-9901

Matthew B. Hillyer − *US Department of Agriculture, Agricultural Research Service, Southern Regional Research Center, New Orleans, Louisiana 70124, United States;* orcid.org/0000-0002-3960-7657

Isabel M. Lima − *US Department of Agriculture, Agricultural Research Service, Southern Regional Research Center, New Orleans, Louisiana 70124, United States*

Sunghyun Nam − *US Department of Agriculture, Agricultural Research Service, Southern Regional Research Center, New Orleans, Louisiana 70124, United States;* orcid.org/0000-0002-4059-606X

Complete contact information is available at: https://pubs.acs.org/10.1021/acsabm.3c00885

Author Contributions

[§]These authors contributed equally: M.W.E., J.H.J. J.H.J., M.W.E., and J.V.E. drafted the manuscript; M.W.E prepared the biosensor substrates; N.T.P. and J.H.J performed the enzymatic assays; J.H.J. analyzed the XRD, performed the kinetic analysis, and drafted the Supporting Information; J.V.E., M.W.E., and J.H.J. conceived the project; J.V.E. directed the project; M.B.H., I.M.L., R.A.D., J.H.J., and S.N. performed the experiments and analyzed the data. All authors have given approval to the final version of the manuscript.

Notes

The authors declare no competing financial interest.

■ ACKNOWLEDGMENTS

This research was supported in part by an appointment to the Agricultural Research Service (ARS) Research Participation Program administered by the Oak Ridge Institute for Science and Education (ORISE) through an interagency agreement between the U.S. Department of Energy (DOE) and the U.S. Department of Agriculture (USDA). ORISE is managed by ORAU under DOE contract number DE-SC0014664. All opinions expressed in this paper are the author's and do not necessarily reflect the policies and views of USDA, DOE, or ORAU/ORISE. This research was supported by the U.S. Department of Agriculture, Agricultural Research Service. Mention of trade names or commercial products in this publication is solely for the purpose of providing specific information and does not imply recommendation or endorsement by the U.S. Department of Agriculture. USDA is an equal opportunity provider and employer.

■ REFERENCES

(1) Ling, Z.; Xu, F.; Edwards, J. V.; Prevost, N. T.; Nam, S.; Condon, B. D.; French, A. D. Nanocellulose as a colorimetric biosensor for effective and facile detection of human neutrophil elastase. *Carbohydr. Polym.* **2019**, *216*, 360−368.

(2) Langari, M. M.; Nikzad, M.; Labidi, J. Nanocellulose-based sensors in medical/clinical applications: The state-of-the-art review. *Carbohydr. Polym.* **2023**, *304*, 120509.

(3) Horta-Velázquez, A.; Morales-Narváez, E. Nanocellulose in wearable sensors. *Green Analytical Chemistry* **2022**, *1*, 100009.

(4) Kamel, S.; A. Khattab, T. Recent Advances in Cellulose-Based Biosensors for Medical Diagnosis. *Biosensors* **2020**, *10* (6), 67.

(5) Solin, K.; Beaumont, M.; Borghei, M.; Orelma, H.; Mertens, P.; Rojas, O. J. Immobilized cellulose nanospheres enable rapid antigen detection in lateral flow immunoassays. *Cellulose* **2023**, *30* (4), 2353−2365.

(6) Edwards, J. V.; Prevost, N.; French, A.; Concha, M.; DeLucca, A.; Wu, Q. Nanocellulose-Based Biosensors: Design, Preparation, and Activity of Peptide-Linked Cotton Cellulose Nanocrystals Having Fluorimetric and Colorimetric Elastase Detection Sensitivity. *Engineering* **2013**, *05* (09), 20−28.

(7) Frazier, T.; Alarcon, A.; Wu, X.; Mohiuddin, O. A.; Motherwell, J. M.; Carlsson, A. H.; Christy, R. J.; Edwards, J. V.; Mackin, R. T.;

Prevost, N.; Gloster, E.; Zhang, Q.; Wang, G.; Hayes, D. J.; Gimble, J. M. Clinical Translational Potential in Skin Wound Regeneration for Adipose-Derived, Blood-Derived, and Cellulose Materials: Cells, Exosomes, and Hydrogels. *Biomolecules* **2020**, *10* (10), 1373.
(8) Hao, L. T.; Park, S.; Choy, S.; Kim, Y. M.; Lee, S. W.; Ok, Y. S.; Koo, J. M.; Hwang, S. Y.; Hwang, D. S.; Park, J.; Oh, D. X. Strong, Multifaceted Guanidinium-Based Adhesion of Bioorganic Nanoparticles to Wet Biological Tissue. *JACS Au* **2021**, *1* (9), 1399−1411.
(9) Liu, C.; Bian, X.; Kwok, R. T. K.; Lam, J. W. Y.; Han, L.; Tang, B. Z. Biological Synthesis and Process Monitoring of an Aggregation-Induced Emission Luminogen-Based Fluorescent Polymer. *JACS Au* **2022**, *2* (9), 2162−2168.
(10) Solin, K.; Orelma, H.; Borghei, M.; Vuoriluoto, M.; Koivunen, R.; Rojas, O. J. Two-Dimensional Antifouling Fluidic Channels on Nanopapers for Biosensing. *Biomacromolecules* **2019**, *20* (2), 1036−1044.
(11) Palamand, S.; Brenden, R. A.; Reed, A. M. Intelligent wound dressings and their physical characteristics. *Wounds: Compend Clin Res. Pract* **1992**, *3*, 149−156.
(12) Edwards, J. V.; Yager, D. R.; Cohen, I. K.; Diegelmann, R. F.; Montante, S.; Bertoniere, N.; Bopp, A. F. Modified cotton gauze dressings that selectively absorb neutrophil elastase activity in solution. *Wound Repair Regen* **2001**, *9* (1), 50−58.
(13) Edwards, J. V.; Howley, P.; Yachmenev, V.; Lambert, A.; Condon, B. Development of a Continuous Finishing Chemistry Process for Manufacture of a Phosphorylated Cotton Chronic Wound Dressing. *Journal of Industrial Textiles* **2009**, *39* (1), 27−43.
(14) Ajami, S.; Khaleghi, L. A review on equipped hospital beds with wireless sensor networks for reducing bedsores. *J. Res. Med. Sci.* **2015**, *20* (10), 1007−1015.
(15) Protease Modulating Dressings. https://www.woundcarehandbook.com/configuration/categories/wound-care/protease-modulating-dressings/ (accessed April 2023).
(16) Fontenot, K. R.; Edwards, J. V.; Haldane, D.; Pircher, N.; Liebner, F.; Condon, B. D.; Qureshi, H.; Yager, D. Designing cellulosic and nanocellulosic sensors for interface with a protease sequestrant wound-dressing prototype: Implications of material selection for dressing and protease sensor design. *J. Biomater Appl.* **2017**, *32* (5), 622−637.
(17) Mackin, R. T.; Fontenot, K. R.; Edwards, J. V.; Prevost, N. T.; Jordan, J. H.; Easson, M. W.; Condon, B. D.; French, A. D. Detection of Human Neutrophil Elastase by Fluorescent Peptide Sensors Conjugated to TEMPO-Oxidized Nanofibrillated Cellulose. *Int. J. Mol. Sci.* **2022**, *23* (6), 3101.
(18) Fontenot, K. R.; Edwards, J. V.; Haldane, D.; Graves, E.; Citron, M. S.; Prevost, N. T.; French, A. D.; Condon, B. D. Human neutrophil elastase detection with fluorescent peptide sensors conjugated to cellulosic and nanocellulosic materials: part II, structure/function analysis. *Cellulose* **2016**, *23* (2), 1297−1309.
(19) Cregge, R. J.; Durham, S. L.; Farr, R. A.; Gallion, S. L.; Hare, C. M.; Hoffman, R. V.; Janusz, M. J.; Kim, H. O.; Koehl, J. R.; Mehdi, S.; Metz, W. A.; Peet, N. P.; Pelton, J. T.; Schreuder, H. A.; Sunder, S.; Tardif, C. Inhibition of human neutrophil elastase. 4. Design, synthesis, X-ray crystallographic analysis, and structure-activity relationships for a series of P2-modified, orally active peptidyl pentafluoroethyl ketones. *J. Med. Chem.* **1998**, *41* (14), 2461−2480.
(20) von Nussbaum, F.; Li, V. M. Neutrophil elastase inhibitors for the treatment of (cardio)pulmonary diseases: Into clinical testing with pre-adaptive pharmacophores. *Bioorg. Med. Chem. Lett.* **2015**, *25* (20), 4370−4381.
(21) Janoff, A.; Blondin, J. Depletion of cartilage matrix by a neutral protease fraction of human leukocyte lysosomes. *Proc. Soc. Exp Biol. Med.* **1970**, *135* (2), 302−306.
(22) Mackin, R. T.; Fontenot, K. R.; Edwards, J. V.; Prevost, N. T.; Grimm, C.; Condon, B. D.; Liebner, F.; Jordan, J. H.; Easson, M. W.; French, A. D. Synthesis and characterization of TEMPO-oxidized peptide-cellulose conjugate biosensors for detecting human neutrophil elastase. *Cellulose* **2022**, *29* (2), 1293−1305.
(23) Sinha, S.; Watorek, W.; Karr, S.; Giles, J.; Bode, W.; Travis, J. Primary structure of human neutrophil elastase. *Proc. Natl. Acad. Sci. U. S. A.* **1987**, *84* (8), 2228−2232.
(24) Sun, Q.; Li, X.; Guo, Y.; Qiu, Y.; Luo, X.; Liu, G.; Han, Y. Coumarin-based turn-on fluorescence probe with a large Stokes shift for detection of endogenous neutrophil elastase in live cells and zebrafish. *Spectrochim Acta A Mol. Biomol Spectrosc* **2022**, *281*, 121563.
(25) Wildeboer, D.; Jeganathan, F.; Price, R. G.; Abuknesha, R. A. Characterization of bacterial proteases with a panel of fluorescent peptide substrates. *Anal. Biochem.* **2009**, *384* (2), 321−328.
(26) Patel, S. A critical review on serine protease: Key immune manipulator and pathology mediator. *Allergol Immunopathol (Madr)* **2017**, *45* (6), 579−591.
(27) Beggiato, M.; Payen, H.; Dupont-Gillain, C.; Krishnamoorthy, S. Impact of tether length and flexibility on the efficiency of analyte capture by tethered receptors. *Sensors and Actuators Reports* **2023**, *5*, 100148.
(28) Wasilewski, T.; Neubauer, D.; Wojciechowski, M.; Szulczynski, B.; Gebicki, J.; Kamysz, W. Evaluation of Linkers' Influence on Peptide-Based Piezoelectric Biosensors' Sensitivity to Aldehydes in the Gas Phase. *Int. J. Mol. Sci.* **2023**, *24* (13), 10610.
(29) González-Fernández, E.; Staderini, M.; Avlonitis, N.; Murray, A. F.; Mount, A. R.; Bradley, M. Effect of spacer length on the performance of peptide-based electrochemical biosensors for protease detection. *Sens. Actuators, B* **2018**, *255*, 3040−3046.
(30) Edwards, J. V.; Prevost, N. T.; French, A. D.; Concha, M.; Condon, B. D. Kinetic and structural analysis of fluorescent peptides on cotton cellulose nanocrystals as elastase sensors. *Carbohydr. Polym.* **2015**, *116*, 278−285.
(31) Krul, E. S. Calculation of Nitrogen-to-Protein Conversion Factors: A Review with a Focus on Soy Protein. *Journal of the American Oil Chemists Society* **2019**, *96* (4), 339−364.
(32) Nishiyama, Y.; Langan, P.; Chanzy, H. Crystal structure and hydrogen-bonding system in cellulose Ibeta from synchrotron X-ray and neutron fiber diffraction. *J. Am. Chem. Soc.* **2002**, *124* (31), 9074−9082.
(33) Ling, Z.; Wang, T.; Makarem, M.; Santiago Cintron, M.; Cheng, H. N.; Kang, X.; Bacher, M.; Potthast, A.; Rosenau, T.; King, H.; et al. Effects of ball milling on the structure of cotton cellulose. *Cellulose* **2019**, *26* (1), 305−328.
(34) Puchowicz, D.; Giesz, P.; Kozanecki, M.; Cieslak, M. Surface-enhanced Raman spectroscopy (SERS) in cotton fabrics analysis. *Talanta* **2019**, *195*, 516−524.
(35) Zou, Y.; Razmkhah, K.; Chmel, N. P.; Hamley, I. W.; Rodger, A. Spectroscopic signatures of an Fmoc-tetrapeptide, Fmoc and fluorene. *Rsc Advances* **2013**, *3* (27), 10854−10858.
(36) Huang, J.; Liang, P.; Xu, J.; Wu, Y.; Shen, W.; Xu, B.; Zhang, D.; Xia, J.; Zhuang, S. Qualitative and quantitative determination of coumarin using surface-enhanced Raman spectroscopy coupled with intelligent multivariate analysis. *Rsc Advances* **2017**, *7* (77), 49097−49101.
(37) Ravikovitch, P. I.; Haller, G. L.; Neimark, A. V. Density functional theory model for calculating pore size distributions: pore structure of nanoporous catalysts. *Adv. Colloid Interface Sci.* **1998**, *76*, 203−226.
(38) Neimark, A. V.; Ravikovitch, P. I.; Vishnyakov, A. Bridging scales from molecular simulations to classical thermodynamics: density functional theory of capillary condensation in nanopores. *J. Phys.: Condens. Matter* **2003**, *15* (3), 347−365.
(39) Ravikovitch, P. I.; Domhnaill, S. C. O.; Neimark, A. V.; Schueth, F.; Unger, K. K. Capillary hysteresis in nanopores: Theoretical and experimental studies of nitrogen adsorption on MCM-41. *Langmuir* **1995**, *11* (12), 4765−4772.
(40) Mo, W.; Li, B.; Liu, J.; Kong, F.; Chen, K. Short-term thermal drying-induced pore expansion effects of cellulosic fibers and its applications. *Cellulose* **2023**, *30* (1), 183−199.
(41) Miri, S.; De Girolamo, A.; Nadeem, H.; Chin, B. W. X.; Hora, Y.; Andrews, P. C.; Batchelor, W. Composite membranes of cellulose-

https://doi.org/10.1021/acsabm.3c00885
ACS Appl. Bio Mater. 2024, 7, 1490−1500

mesoporous silica: optimization of membrane fabrication and adsorption capacity. *Cellulose* **2023**, *30* (1), 339−357.
(42) Lan, G.-X.; Liu, Y.; Zhou, N.; Guo, D.-Q.; Ma, M.-G. Multifunctional nanocellulose-based composites for potential environmental applications. *Cellulose* **2023**, *30* (1), 39−60.
(43) Bae, Y. S.; Yazaydin, A. O.; Snurr, R. Q. Evaluation of the BET method for determining surface areas of MOFs and zeolites that contain ultra-micropores. *Langmuir* **2010**, *26* (8), 5475−5483.
(44) Jordan, J. H.; Easson, M. W.; Condon, B. D. Alkali Hydrolysis of Sulfated Cellulose Nanocrystals: Optimization of Reaction Conditions and Tailored Surface Charge. *Nanomaterials* **2019**, *9* (9), 1232.
(45) Luo, J.; Semenikhin, N.; Chang, H.; Moon, R. J.; Kumar, S. Post-sulfonation of cellulose nanofibrils with a one-step reaction to improve dispersibility. *Carbohydr. Polym.* **2018**, *181*, 247−255.
(46) Jiang, F.; Hsieh, Y. L. Assembling and redispersibility of rice straw nanocellulose: effect of tert-butanol. *ACS Appl. Mater. Interfaces* **2014**, *6* (22), 20075−20084.
(47) Edwards, J. V.; Fontenot, K.; Liebner, F.; Pircher, N. D. N.; French, A. D.; Condon, B. D. Structure/Function Analysis of Cotton-Based Peptide-Cellulose Conjugates: Spatiotemporal/Kinetic Assessment of Protease Aerogels Compared to Nanocrystalline and Paper Cellulose. *Int. J. Mol. Sci.* **2018**, *19* (3), 840.
(48) Cullen, W.; Metherell, A. J.; Wragg, A. B.; Taylor, C. G. P.; Williams, N. H.; Ward, M. D. Catalysis in a Cationic Coordination Cage Using a Cavity-Bound Guest and Surface-Bound Anions: Inhibition, Activation, and Autocatalysis. *J. Am. Chem. Soc.* **2018**, *140* (8), 2821−2828.
(49) Leatherbarrow, R. J. Use of nonlinear regression to analyze enzyme kinetic data: application to situations of substrate contamination and background subtraction. *Anal. Biochem.* **1990**, *184* (2), 274−278.
(50) Duggleby, R. G., [3] Analysis of enzyme progress curves by nonlinear regression. In *Methods in Enzymology*; Academic Press: 1995; Vol. *249*, pp 61−90.
(51) Jordan, J. H.; Easson, M. W.; Thompson, S.; Wu, Q.; Condon, B. D. Lignin-containing cellulose nanofibers with gradient lignin content obtained from cotton gin motes and cotton gin trash. *Cellulose* **2021**, *28* (2), 757−773.
(52) Touzinsky, G. F.; Gordon, S. H. Degree of Substitution of Cellulose Derivatives Containing N Different Substituent Groups. *Carbohydr. Res.* **1979**, *69* (Mar), 327−329.
(53) French, A. D. Glucose, not cellobiose, is the repeating unit of cellulose and why that is important. *Cellulose* **2017**, *24* (11), 4605−4609.
(54) Nam, S.; Easson, M.; Jordan, J. H.; He, Z.; Zhang, H.; Santiago Cintron, M.; Chang, S. Unveiling the Hidden Value of Cotton Gin Waste: Natural Synthesis and Hosting of Silver Nanoparticles. *ACS Omega* **2023**, *8* (34), 31281−31292.
(55) Ling, Z.; Edwards, J. V.; Guo, Z.; Prevost, N. T.; Nam, S.; Wu, Q.; French, A. D.; Xu, F. Structural variations of cotton cellulose nanocrystals from deep eutectic solvent treatment: micro and nano scale. *Cellulose* **2019**, *26* (2), 861−876.
(56) French, A. D. Idealized powder diffraction patterns for cellulose polymorphs. *Cellulose* **2014**, *21* (2), 885−896.
(57) Nam, S.; French, A. D.; Condon, B. D.; Concha, M. Segal crystallinity index revisited by the simulation of X-ray diffraction patterns of cotton cellulose Ibeta and cellulose II. *Carbohydr. Polym.* **2016**, *135*, 1−9.
(58) Nam, S.; Hillyer, M. B.; Condon, B. D. Method for identifying the triple transition (glass transition-dehydration-crystallization) of amorphous cellulose in cotton. *Carbohydr. Polym.* **2020**, *228*, 115374.

https://doi.org/10.1021/acsabm.3c00885
ACS Appl. Bio Mater. 2024, 7, 1490−1500